chemosensors

Article

Electrochemical Sensing of Hg^{2+} Ions Using an SWNTs/Ag@ZnBDC Composite with Ultra-Low Detection Limit

Gajanan A. Bodkhe [1], Bhavna Hedau [2], Mayuri S. More [2], Myunghee Kim [1,*] and Mahendra D. Shirsat [2,*]

[1] Department of Food Science and Technology, Yeungnam University, Gyeongsan 38541, Gyeongsangbuk-do, Republic of Korea; gabodkhe@gmail.com
[2] RUSA Center for Advanced Sensor Technology, Department of Physics, Dr. Babasaheb Ambedkar Marathwada University, Chhatrapati Sambhajinagar (Aurangabad) 431004, India; hedaubhavna@outlook.com (B.H.); mayurimore098@gmail.com (M.S.M.)
* Correspondence: foodtech@ynu.ac.kr (M.K.); mdshirsat@bamu.ac.in (M.D.S.)

Abstract

A novel single-walled carbon nanotube (SWNT), silver (Ag) nanoparticle, and zinc benzene carboxylate (ZnBDC) metal–organic framework (MOF) composite was synthesised and systematically characterised to develop an efficient platform for mercury ion (Hg^{2+}) detection. X-ray diffraction confirmed the successful incorporation of Ag nanoparticles and SWNTs without disrupting the crystalline structure of ZnBDC. Meanwhile, field-emission scanning electron microscopy and energy-dispersive spectroscopy mapping revealed a uniform elemental distribution. Thermogravimetric analysis indicated enhanced thermal stability. Electrochemical measurements (cyclic voltammetry and electrochemical impedance spectroscopy) demonstrated improved charge transfer properties. Electrochemical sensing investigations using differential pulse voltammetry revealed that the SWNTs/Ag@ZnBDC-modified glassy carbon electrode exhibited high selectivity toward Hg^{2+} ions over other metal ions (Cd^{2+}, Co^{2+}, Cr^{3+}, Fe^{3+}, and Zn^{2+}), with optimal performance at pH 4. The sensor displayed a linear response in the concentration range of 0.1–1.0 nM (R^2 = 0.9908), with a calculated limit of detection of 0.102 nM, slightly close to the lowest tested point, confirming its high sensitivity for ultra-trace Hg^{2+} detection. The outstanding sensitivity, selectivity, and reproducibility underscore the potential of SWNTs/Ag@ZnBDC as a promising electrochemical platform for detecting trace levels of Hg2+ in environmental monitoring.

Keywords: single-walled carbon nanotubes; electrochemical sensor; Hg^{2+} ions; Ag nanoparticles; metal–organic frameworks

check for updates

Received: 8 June 2025
Revised: 11 July 2025
Accepted: 14 July 2025
Published: 16 July 2025

Citation: Bodkhe, G.A.; Hedau, B.; More, M.S.; Kim, M.; Shirsat, M.D. Electrochemical Sensing of Hg^{2+} Ions Using an SWNTs/Ag@ZnBDC Composite with Ultra-Low Detection Limit. *Chemosensors* **2025**, *13*, 259. https://doi.org/10.3390/chemosensors13070259

Copyright: © 2025 by the authors. Licensee MDPI, Basel, Switzerland. This article is an open access article distributed under the terms and conditions of the Creative Commons Attribution (CC BY) license (https://creativecommons.org/licenses/by/4.0/).

1. Introduction

The increased industrialisation and anthropogenic activities over recent decades have led to the persistent release of hazardous heavy metal ions (HMIs) into water systems [1–3]. They can exist in the form of metallic, inorganic, or organic mercury (Hg). Among them, the mercury ion (Hg^{2+}) is of particular concern, even when present at trace levels, due to its significant risks to human health, including neurological, renal, and developmental impairments, as well as its notable link to disorders such as Minamata disease. Therefore, reliable, rapid, and sensitive detection methods are urgently required to monitor Hg^{2+} levels in environmental samples and mitigate potential health impacts.

Electrochemical sensing techniques have gained increasing interest as effective tools for HMI detection due to their low cost, simplicity, portability, and excellent analytical

sensitivity [4]. Among them, differential pulse voltammetry (DPV) is particularly advantageous for trace analysis because of its high current resolution and minimal background noise. However, the sensitivity and selectivity of electrochemical sensors largely depend on the properties of the sensing interface, particularly the availability of active sites, electron transfer capability, and affinity toward target ions [5,6].

To enhance these properties, recent research has focused on integrating conductive carbon nanostructures with functional metal–organic frameworks (MOFs) [7]. Owing to their modular structures, high porosity, and versatile surface chemistry, MOFs serve as excellent platforms for metal ion adsorption. Nevertheless, their poor intrinsic conductivity can limit electrochemical performance [8–10]. A promising strategy to address this involves the fabrication of hybrid materials combining MOFs with conductive nanomaterials like single-walled carbon nanotubes (SWNTs) and catalytically active nanoparticles, such as silver (Ag) nanoparticles (Ag NPs) [11,12].

In this study, we present a hybrid material, SWNTs/Ag incorporated zinc benzene carboxylate (ZnBDC) MOF composite (SWNTs/Ag@ZnBDC), designed for the selective and sensitive detection of Hg^{2+} using DPV at pH 4. The ZnBDC MOF serves as a stable, porous matrix with favourable coordination sites for Hg^{2+}, while AgNPs enhance electron transfer and electrocatalytic response [13,14]. The inclusion of SWNTs significantly improves electrical conductivity and surface area, facilitating rapid charge transport and enhanced signal amplification. The synergistic combination of these components creates a highly responsive and stable sensing interface capable of operating under mild acidic conditions. We also investigate the electrochemical behaviour of this composite toward Hg^{2+} detection and optimise critical parameters, including deposition time, deposition voltage, pH of the supporting electrolyte, and the potential range. The prepared SWNTs/Ag@ZnBDC/GCE-based sensor demonstrates excellent analytical performance, including a low detection limit, a wide linear range, high repeatability, and excellent selectivity in the presence of potentially interfering metal ions. Compared to conventional mercury-film and bismuth-film electrodes, which offer good sensitivity but pose environmental and handling concerns, the SWNTs/Ag@ZnBDC composite provides a mercury-free platform with enhanced selectivity, superior conductivity, and structural stability. Traditional electrodes often lack molecular recognition capabilities, whereas MOF-based hybrids can be tailored for specific interactions, enhancing sensitivity and reproducibility. This work provides valuable insight into the design of multifunctional MOF-based hybrid sensors for environmental monitoring and real-world water quality applications.

2. Experimental

2.1. Reagents and Materials

Zinc nitrate hexahydrate, cadmium nitrate tetrahydrate, cobalt nitrate hexahydrate, mercuric chloride, iron(III) nitrate nonahydrate, lead nitrate, AgNPs, copper nitrate trihydrate, N, N-dimethylformamide (DMF), potassium chloride (KCl), sulfuric acid (H_2SO_4), and standard pH buffer solutions were purchased from Molychem, Mumbai, India. SWNTs were obtained from Techinstro Industries, Nagpur, India. Terephthalic acid (H_2BDC) was procured from Sigma-Aldrich (St. Louis, MO, USA).

2.2. Synthesis of ZnBDC and SWNTs/Ag@ZnBDC Composites

ZnBDC MOF was prepared following a previously reported procedure with slight modifications [15]. In a typical synthesis, 1.296 g of H_2BDC and 5.824 g of zinc nitrate hexahydrate were separately dissolved in 140 mL DMF. The two solutions were combined and stirred for 30 min at room temperature to ensure complete homogenisation. The

mixture was then kept in a 250 mL Teflon-lined autoclave and heated for 24 h at 120 °C in an oven.

For the preparation of the SWNTs/Ag@ZnBDC composite, 400 mg of AgNPs and 2 mg of SWNTs were first dispersed separately in 3 mL of DMF and sonicated for 60 min to achieve a uniform dispersion. The ratio of 400 mg AgNPs to 2 mg SWNTs was selected based on prior literature [16], where similar compositions were found to provide improved electrical conductivity and uniform particle dispersion within MOF composites. These AgNP and SWNT dispersions were then added to the ZnBDC precursor solution, followed by further stirring and sonication. The combined mixture was transferred to a separate 250 mL Teflon-lined autoclave and subjected to the same heating conditions (120 °C, 24 h).

After automatic cooling to room temperature, the resulting white crystalline products—ZnBDC and SWNTs/Ag@ZnBDC—were collected and washed thoroughly with DMF. To facilitate solvent exchange, the samples were soaked in chloroform. Finally, the materials were dried in an oven at 60 °C and activated at 120 °C to remove any residual solvent molecules. The activated composites were stored in airtight containers until further use.

2.3. Fabrication of Electrochemical Sensor and Electrode

Electrochemical sensor probes were fabricated by modifying glassy carbon electrodes (GCE) with either pure ZnBDC or SWNTs/Ag@ZnBDC composites. Before modification, the GCE surfaces were polished sequentially using alumina slurries of 0.1, 0.3, and 0.05 μm particle sizes to achieve a mirror-like finish. The polished electrodes were thoroughly rinsed with deionised (DI) water, followed by sonication in acetone and DI water to remove any residual contaminants.

The electrodes were then electrochemically activated by cyclic voltammetry (CV) in 0.5 M aqueous H_2SO_4 solution, scanning from −0.4 to 1.5 V at a scan rate of 0.05 V/s. Activation was continued until stable and reproducible voltammograms were obtained. For sensor fabrication, a suspension of ZnBDC or SWNTs/Ag@ZnBDC (5 mg/mL) was prepared by dispersing the material in a 4:1 (v/v) mixture of acetone and Nafion. A 5 μL aliquot of the suspension was drop-cast onto the pretreated GCE surface and allowed to dry at room temperature. The modified electrodes were then used for all subsequent electrochemical measurements.

2.4. Electrochemical Measurements

Electrochemical impedance spectroscopy (EIS) and CV analyses of the ZnBDC and SWNTs/Ag@ZnBDC sensor probes were conducted using a CHI 660C electrochemical workstation (CH Instruments, Bee Cave, TX, USA). Both measurements were performed in 0.1 M KCl solution. EIS data were recorded using a 5 mV AC amplitude at an initial potential of 0 V across a frequency range of 0.01 to 100 kHz. CV measurements were performed at a scan rate of 0.1 V/s within a potential window of −0.8 to 0.5 V. Sensing experiments were carried out using the DPV technique in 0.1 M acetate buffer (pH 4.0), a solution selected to match the optimal redox potential range for each targeted HMI. DPV measurements were conducted using an increment potential of 4 mV, a pulse amplitude of 50 mV, a pulse width of 50 ms, a sampling width of 16.7 ms, and the accumulation time was set to 300 s over a potential window from −0.1 V to 0.7 V.

2.5. Material Characterisations

Fourier-transform infrared (FTIR) spectroscopy measurements were performed in the range of 500–4000 cm^{-1} using a Bruker Alpha FTIR spectrometer (Bruker, Rheinstetten, Germany) equipped with a ZnSe-ATR accessory. X-ray diffraction (XRD) patterns were collected on a Bruker D8 Advance diffractometer (Bruker) in Bragg–Brentano reflection geometry, employing Cu-Kα radiation (λCu = 1.54 Å) with a Cu tube current of 40 mA

and an accelerating voltage of 40 kV. Surface morphology and elemental composition were analysed by field emission scanning electron microscopy (FESEM) using a MIRA3 LMH microscope (TESCAN, Brno, Czech Republic) coupled with energy-dispersive X-ray spectroscopy (EDS) (Oxford Instruments, Abingdon, UK). Prior to measurement, the samples were degassed at 155 °C for 8 h. All electrochemical characterisations and sensing measurements were carried out using a CHI 660C electrochemical workstation (CH Instruments, Bee Cave, TX, USA). Thermogravimetric analysis (TGA) was performed with a DTG-60H analyser (Shimadzu Corp., Kyoto, Japan) under a nitrogen atmosphere at a heating rate of 10 °C/min.

3. Results and Discussion

3.1. Material Analysis

The FTIR spectra of ZnBDC MOF and SWNTs/Ag@ZnBDC composite are shown in Figure 1a. In the spectrum of ZnBDC MOF, distinct absorption bands are observed at 1376 and 1574 cm^{-1}, corresponding to the symmetric and asymmetric stretching vibrations of Zn^{2+}-coordinated carboxylate (C–O) groups, respectively [17]. The region between 640 and 900 cm^{-1} exhibits characteristic peaks associated with out-of-plane bending vibrations of aromatic C–H bonds from the H_2BDC linker [17]. Additionally, sharp bands between 941 and 1254 cm^{-1} are attributed to in-plane bending vibrations of the linker [17].

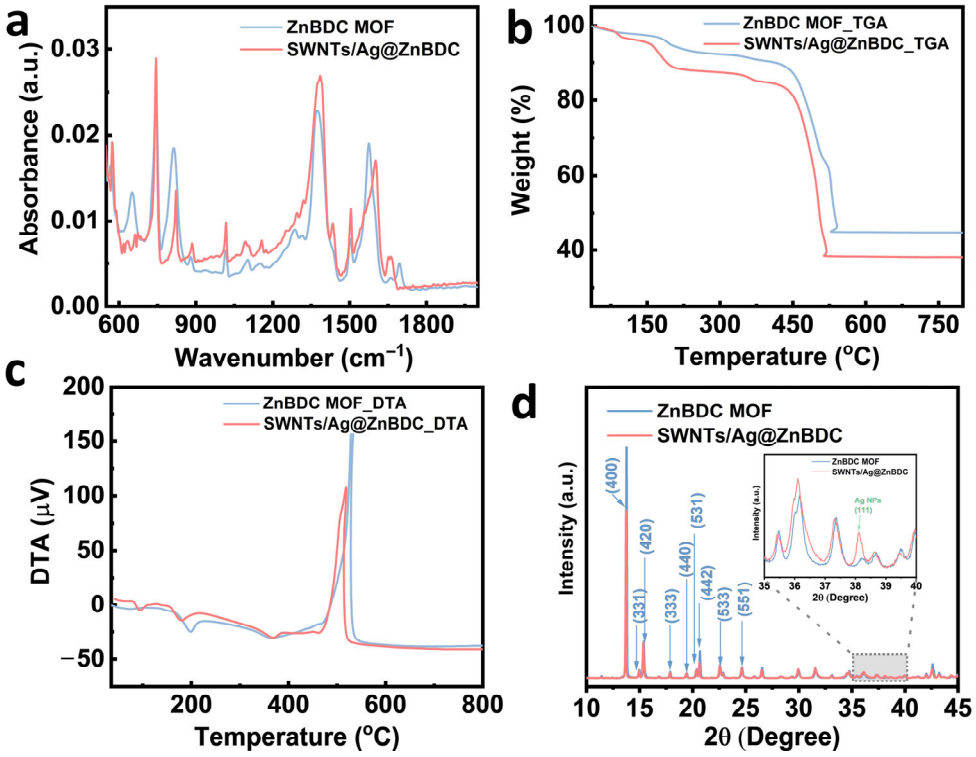


Figure 1. (**a**) FTIR spectra, (**b**,**c**) TGA/DTA curves, and (**d**) XRD spectra of ZnBDC and SWNTs/Ag@ZnBDC.

After the formation of the SWNTs/Ag@ZnBDC composite, most of the basic vibrational peaks of the pure ZnBDC MOF are largely preserved, which shows that the structural integrity of the framework remains intact. However, several notable changes are evident. A shift in the symmetric stretching band from 1376 to 1382 cm^{-1} and in the asymmetric stretching band from 1574 to 1600 cm^{-1} is observed, which suggests the interactions between the carboxylate groups of MOFs and the AgNPs. Moreover, the C–O stretching band shifts from 1282 to 1291 cm^{-1}, further supporting the involvement of Ag in the coordination environment. New peaks appearing at 1433, 1453, 1543, 1558, and 1650 cm^{-1}

in the composite spectrum provide additional evidence of chemical interactions between AgNPs and the ZnBDC framework. In the lower wavenumber region (640–900 cm^{-1}), a reduction in intensity and slight shifts in the out-of-plane C–H bending peaks are observed, indicative of perturbations in the aromatic ring environment, likely due to π–π stacking interactions with SWNTs. Broadening and baseline elevation in the 941–1254 cm^{-1} region further suggest that the incorporation of SWNTs and AgNPs induces disorder in the local vibrational environment of the MOF. Collectively, these spectral changes confirm the successful formation of the SWNTs/Ag@ZnBDC composite while maintaining the essential framework of ZnBDC MOF.

The thermal stability of the ZnBDC MOF and the SWNTs/Ag@ZnBDC composite was assessed by TGA and differential thermal analysis (DTA), and the results are shown in Figure 1b,c. The TGA curves reveal an initial weight loss below 170 °C for both samples, corresponding to the removal of physisorbed water and residual solvent molecules. The ZnBDC MOF exhibits gradual decomposition up to 450 °C, followed by a sharp weight loss between 450 and 530 °C, indicative of the breakdown of the organic linker and collapse of the MOF. A residual mass of approximately 44% remains at 800 °C, attributable to the formation of ZnO. In comparison, the SWNTs/Ag@ZnBDC composite shows a similar dehydration stage but undergoes decomposition at slightly lower temperatures, with significant weight loss occurring between 440 and 500 °C. The residual mass of the composite is reduced somewhat, consistent with the presence of AgNPs and SWNTs influencing the thermal degradation process.

The DTA profiles further support these observations (Figure 1c). Both materials exhibit an initial endothermic event below 170 °C, attributed to solvent loss. The pristine ZnBDC MOF exhibits a sharp exothermic peak at temperatures ranging from 480 to 530 °C, corresponding to the combustion of the organic framework. For the composite, the exothermic peak shifts slightly to 470–510 °C with reduced intensity, suggesting that the incorporation of SWNTs and AgNPs moderates the decomposition behaviour. The TGA/DTA results confirm that the composite retains substantial thermal stability; the presence of nanomaterials slightly lowers the decomposition temperature and modifies the thermal degradation pathway.

The XRD patterns of the pure ZnBDC MOF and the SWNTs/Ag@ZnBDC composite are presented in Figure 1d. The diffraction peaks observed for ZnBDC are well indexed to the known crystal planes (400), (420), (331), (333), (440), (442), (531), (533), and (551), consistent with previously reported ZnBDC structures, confirming the successful synthesis of a highly crystalline MOF [18,19]. Upon the incorporation of AgNPs and SWNTs, the composite (SWNTs/Ag@ZnBDC) maintains the characteristic diffraction peaks of ZnBDC, indicating that the overall framework structure remains intact. Notably, a new diffraction peak appears at 38.2° (inset), corresponding to the (111) plane of face-centred cubic (fcc) AgNPs, which confirms the successful embedding of AgNPs within the ZnBDC matrix [20]. The slight broadening and reduced intensity of the Ag (111) peak (~38.2°) suggest fine dispersion of AgNPs within the ZnBDC matrix. This is consistent with prior reports, where peak broadening is attributed to reduced crystallite size and uniform nanoparticle distribution due to strain and finite domain effects [17,20,21]. A comparative analysis reveals a slight reduction in crystallinity in the SWNTs/Ag@ZnBDC composite compared to pristine ZnBDC MOF, indicating minor lattice distortion upon the incorporation of AgNPs and SWNTs. Additionally, the crystallite size is expected to increase slightly, reflecting the presence of metallic nanoparticles embedded within the MOF structure. Thus, the XRD analysis confirms that the ZnBDC framework retains its structural integrity post-modification, while the successful introduction of AgNPs is evident through the emergence of Ag-specific diffraction peaks.

The FESEM images (Figure 2) reveal well-defined rectangular plate-like crystals of ZnBDC MOF with smooth surfaces and sharp edges, indicating high crystallinity and morphological integrity [18]. The incorporation of SWNTs can be seen in the enlarged image (Figure 2b inset), and AgNPs do not visibly alter the primary morphology of the MOF (Figure 2a,b). Elemental mapping by EDS confirms the uniform distribution of carbon, zinc, and oxygen elements of the MOF structure (Figure 2c–f). Notably, Ag is detected as discrete, sparsely distributed spots across the particle surface, indicating the successful incorporation of AgNPs without disrupting the crystal architecture. These observations confirm that the SWNTs/Ag@ZnBDC composite maintains the structural features of ZnBDC MOF while integrating functional nanomaterials.

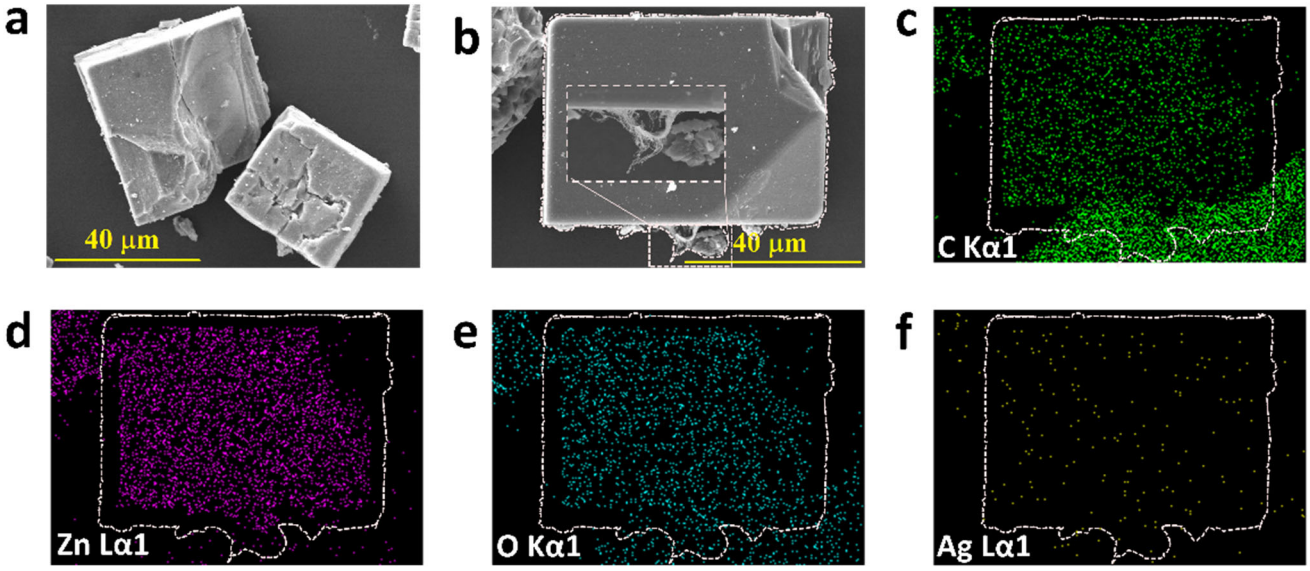


Figure 2. (**a**,**b**) FESEM images of pure ZnBDC and SWNTs/Ag@ZnBDC composite showing preserved plate-like MOF crystals with slight. (**c**–**f**) EDS elemental maps of C, Zn, O, and Ag, confirming uniform distribution of framework elements and discrete AgNPs decoration.

The electrochemical properties of the ZnBDC MOF and the SWNTs/Ag@ZnBDC composite were evaluated by CV and EIS in 0.1 M KCl electrolyte (Figure 3). The CV curves of the ZnBDC MOF exhibit a near-rectangular shape, characteristic of electric double-layer capacitance behaviour at moderate current densities (Figure 3a). In contrast, the SWNTs/Ag@ZnBDC composite shows a similar capacitive profile but with significantly higher current densities across the entire potential window, indicating an enhanced charge storage capability. The CV curves exhibit distinct redox peaks associated with the redox activity of Ag, including an anodic peak near 1.4 V corresponding to the oxidative dissolution of Ag. These features suggest the presence of pseudocapacitive contributions arising from the electroactive Ag component within the composite. The increase in the current response of the SWNTs/Ag@ZnBDC composite is attributed to the synergistic effects of SWNTs and AgNPs, which enhance electrical conductivity and provide additional electroactive sites, thereby facilitating faster electron transport and ion diffusion [22].

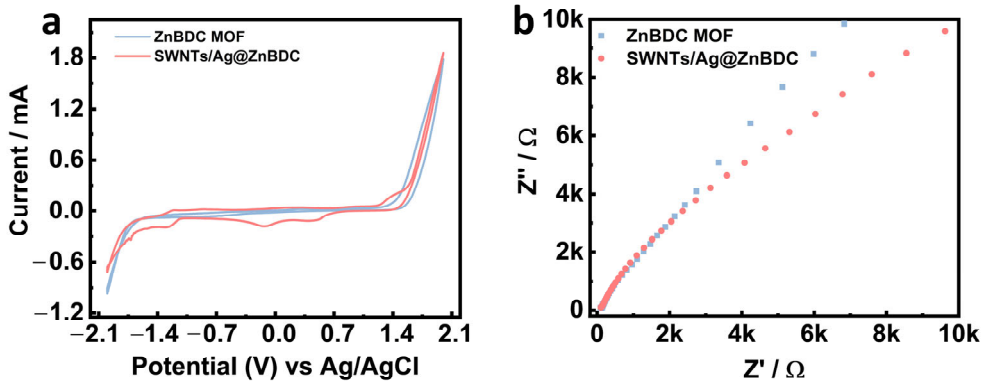


Figure 3. (**a**) Cyclic voltammogram and (**b**) electrochemical impedance spectra of ZnBDC and SWNTs/Ag@ZnBDC.

The EIS measurements further corroborate these findings (Figure 3b). The Nyquist plot of the ZnBDC MOF displays high impedance values, with Z′ reaching up to 10 kΩ, reflecting considerable charge transfer resistance and slow ion diffusion. The slope of the Nyquist plot at low frequencies exceeds 45°, which indicates that the charge transfer process is influenced by ion diffusion limitations. In contrast, ideal capacitive behaviour would be characterised by a slope approaching 90°, representing efficient charge storage with minimal diffusion resistance. At high frequencies, the Nyquist plots of the pristine ZnBDC and the SWNTs/Ag@ZnBDC composite overlap, indicating similar charge transfer resistance. However, in the low-frequency region, the composite exhibits a markedly lower impedance, reflecting improved ion mobility and capacitive characteristics contributed by the presence of SWNTs and AgNPs. Together, these electrochemical results confirm that the SWNTs/Ag@ZnBDC composite exhibits superior electrochemical performance compared to the pristine ZnBDC MOF, making it a promising candidate for capacitive energy storage and sensing applications.

3.2. Electrochemical Sensing Performance of SWNTs/Ag@ZnBDC/GCE

To evaluate the electrochemical sensing performance of prepared SWNTs/Ag@ZnBDC/GCE, DPV was employed for the selective and sensitive detection of various HMIs, including Cd^{2+}, Co^{2+}, Cr^{3+}, Fe^{3+}, Hg^{2+}, and Zn^{2+} under different pH conditions ranging from pH 3 to 10, as shown in Figure 4a–h. The SWNTs/Ag@ZnBDC/GCE exhibited a comparatively distinctive oxidation peak toward Hg^{2+} (Figure 4h) than Cd^{2+}, Co^{2+}, Cr^{3+}, Fe^{3+}, and Zn^{2+} (Figure 4a–g), clearly indicating its high selectivity for Hg^{2+} ions. The pH of the supporting electrolyte has a significant influence on the chemical speciation, solubility, and electrochemical activity of Hg^{2+} ions. At lower pH values, Hg^{2+} exists predominantly in its free ionic form, which is more electrochemically active and readily interacts with the sensor surface. Conversely, at higher pH levels, Hg^{2+} tends to hydrolyse and precipitate as $Hg(OH)_2$, thereby reducing its solubility and availability for redox interactions, which suppresses the sensor signal.

On the other hand, at excessively low pH, hydrogen evolution reactions may interfere with the electrochemical response. Therefore, optimising the pH was essential to ensure Hg^{2+} remains in a stable and detectable ionic form while avoiding interference from background processes. The optimised sensor exhibited a clear dependence of the oxidation peak current on the pH of the supporting electrolyte, with the most intense and well-defined peak observed at a pH of 4. This suggests that the coordination between Hg^{2+} ions and the active sites of ZnBDC, as well as the conductivity enhancement provided by SWNTs, is maximised under mildly acidic conditions. This enhanced sensing activity at pH 4 can be attributed to several factors. At lower pH, Hg^{2+} ions remain predominantly in their free

ionic form, which is more electrochemically active and readily interacts with the electrode surface. In contrast, at higher pH levels, Hg^{2+} tends to hydrolyse or precipitate as $Hg(OH)_2$, thereby reducing its availability and suppressing the sensor response. Thus, pH 4 provides an optimal balance between sufficient proton concentration for efficient proton-coupled electron transfer, minimal background interference, and favourable redox kinetics [23–26]. Therefore, pH 4 was selected for subsequent quantitative detection experiments. Although a background current originating from the redox activity of Ag is present, it does not significantly interfere with the detection of Hg^{2+}. This is attributed to the preferential coordination of Hg^{2+} ions with the active sites of the ZnBDC framework, which facilitates selective sensing despite the presence of electroactive Ag components.

Furthermore, under optimised conditions, the SWNTs/Ag@ZnBDC/GCE was subjected to DPV measurements with increasing concentrations of Hg^{2+} ranging from 0.1 to 1 nM, as shown in Figure 5a. A progressive increase in peak current was observed with increasing Hg^{2+} concentrations, confirming a strong, concentration-dependent electrochemical response and efficient interaction between Hg^{2+} ions and the sensing interface. Figure 5b shows the corresponding calibration, which exhibits excellent linearity with a correlation coefficient (R^2 = 0.9908) close to unity, demonstrating its reliability for quantitative analysis. Furthermore, a plot of the current response calculated as $(I - I_0)/I_0 \times 100$, where I_0 is the baseline current, against Hg^{2+} concentration [27], including error bars (Figure 5c), validated the reproducibility and consistency of the measurements. Figure 5d presents the calibration curve for Hg^{2+} detection using prepared SWNTs/Ag@ZnBDC/GCE at different accumulation times.

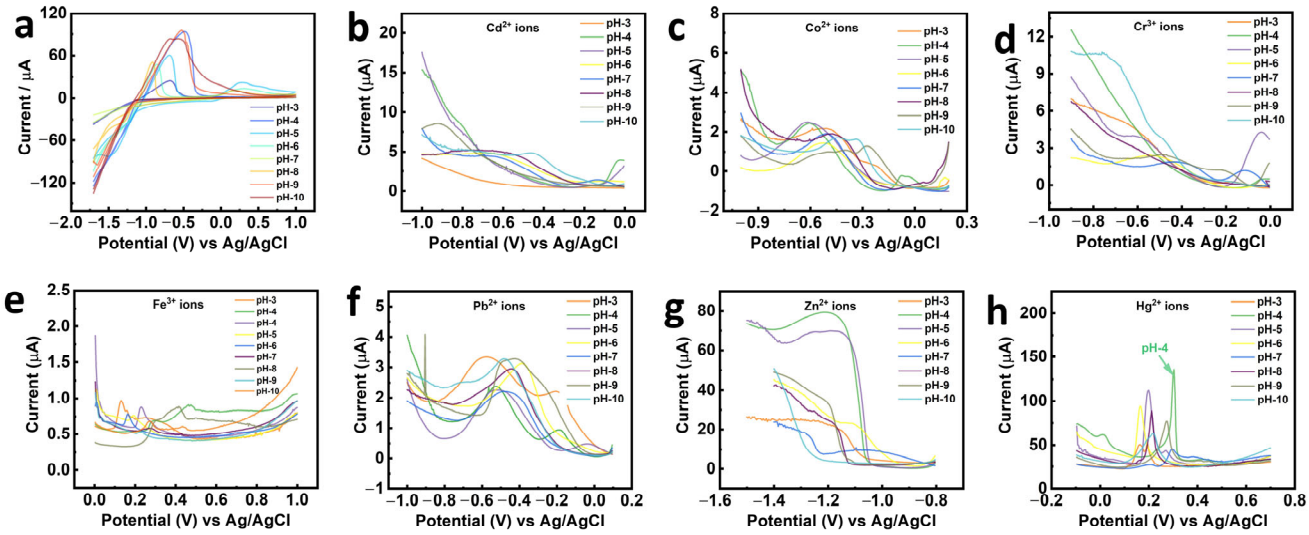


Figure 4. (**a**) SWNTs/Ag@ZnBDC/GCE sensor probe cyclic voltammogram under different pH conditions. pH-dependent selectivity of SWNTs/Ag@ZnBDC/GCE sensor probe for (**b**) Cd^{2+}, (**c**) Co^{2+}, (**d**) Cr^{3+}, (**e**) Fe^{3+}, (**f**) Hg^{2+}, (**g**) Zn^{2+}, and (**h**) Hg^{2+} ions using differential pulse voltammetry (DPV) for 1 µM concentration.

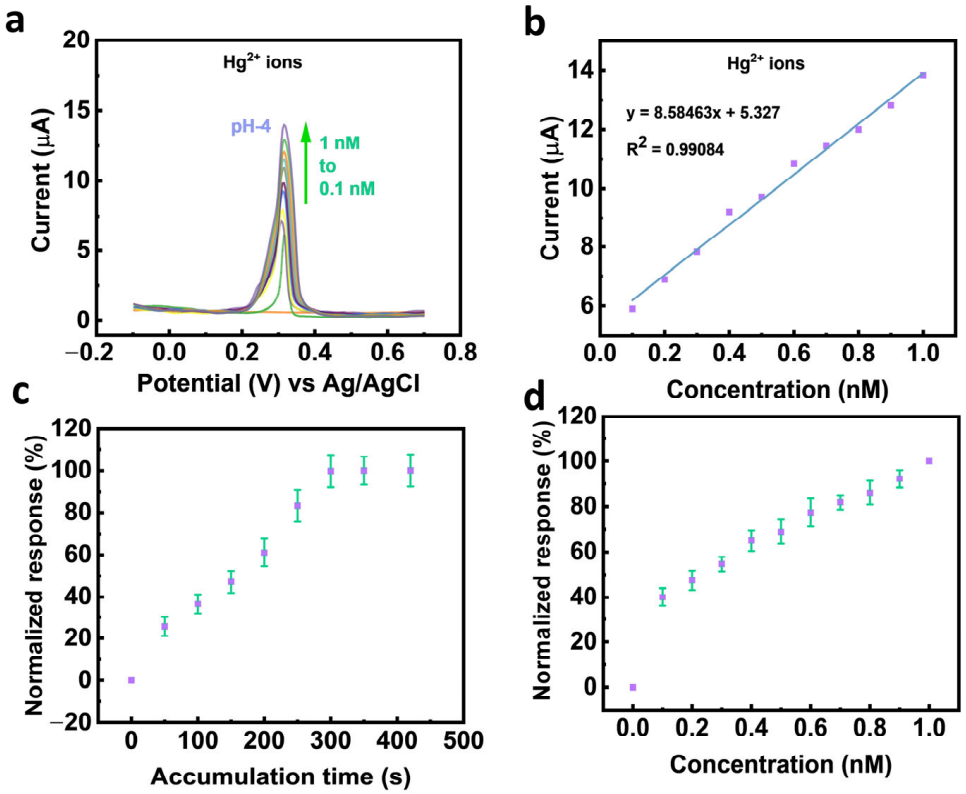


Figure 5. (**a**) Sensor DPV response toward Hg^{2+} ions at pH 4 in the 0.1–1 nM range. (**b**) Calibration plot for Hg^{2+} ions. (**c**) Scatter plot showing normalised sensor response (%), with error bars representing ± standard deviation (SD; n = 3). (**d**) Sensor response at different accumulation times with error bars representing ± SD (n = 3).

For practical applications, accumulation time is a key parameter that influences sensitivity and can be optimised depending on the required detection limit and response time. Figure 5c presents the optimisation curves for Hg^{2+} detection using the SWNTs/Ag@ZnBDC/GCE at different accumulation times. Accumulation time refers to the duration of the preconcentration step before the DPV scan. With increasing accumulation time up to approximately 300 s, there is a significant increase in the current response, as a longer accumulation period allows more Hg^{2+} ions to interact and bind with the active sites of the electrode surface. However, extending the accumulation time beyond the optimal point leads to overcrowding of Hg^{2+} ions on the electrode surface, resulting in saturation, where no further increase in current is observed despite higher ion availability. Thus, the observed linear response up to approximately 300 s demonstrates the effective surface binding kinetics and optimal charge transfer, making this accumulation period ideal for balancing high sensitivity with reasonable analysis time in practical sensing applications. Using these results, the limit of detection (LOD) and limit of quantification (LOQ) were calculated using the standard IUPAC method [28,29]:

$$\mathrm{LOD} = \frac{3\sigma}{m} \quad (1)$$

$$\mathrm{LOQ} = \frac{10\sigma}{m} \quad (2)$$

where σ represents the standard deviation of the blank and m is the slope of the calibration curve. The SWNTs/Ag@ZnBDC/GCE exhibited an impressively low LOD of 0.1 nM and LOQ of 0.39 nM, underscoring its ultra-sensitive detection capability compared to other reported sensors, as shown in Table 1. These values are well below the safety limits

defined by environmental agencies for Hg^{2+} in drinking water, confirming the suitability of this platform for real-world applications. Table 1 depicts the comparative analysis of the LOD for various electrochemical sensors developed for Hg^{2+} detection. This sensor performance shows the effectiveness of integrating SWNTs and AgNPs within the ZnBDC framework, enhancing electron transfer and providing abundant active sites for Hg^{2+} detection. Notably, while the Ag-La-succinate/GCE sensor achieved an LOD of 0.1 nM, the SWNTs/Ag@ZnBDC/GCE sensor offers comparable sensitivity with the added benefits of improved stability and reproducibility due to the synergistic effects of its composite materials. The linear calibration range was observed between 0.1 and 1.0 nM (Figure 5b), while the LOD was calculated to be below 0.1 nM using the IUPAC method, confirming the sensor's high sensitivity even at sub-nanomolar concentrations. Although the sensor demonstrates excellent sensitivity within a narrow linear range (0.1–1 nM), this limited range may constrain its applicability in samples with broader concentration variability. Future studies will focus on expanding the detection range through further electrode optimisation and extended preconcentration times.

Table 1. Comparison of the LOD obtained for the SWNTs/Ag@ZnBDC/GCE sensor with other sensors reported for the electrochemical detection of Hg^{2+}.

Sensing Material	Technique	LOD (nM)	Reference
GCE/Cu-MOF nanocubes	DPV	0.0633	[30]
MB-UiO-66-NH_2/MWCNTs/GC	DPASV	6.42	[31]
Amino-enriched Zn-MOFs	SWASV	2.5	[32]
Cu-MOF	SWASV	1.7	[33]
Ag/SWNTs@CuBTC MOF	DPV	3.03	[16]
AuNPs/mpg-C_3N_4/GCE	DPSV	10.3	[34]
La-doped ZIF+L-cystine	DPV	52	[35]
Ag-La-succinate/GCE	EIS	0.1	[36]
SWNTs@ZnBDC/GCE	CV	6.74	[37]
UiO-66-NHC(S)NHMe/3D-KSC	SWASV	9.4	[38]
GA-UiO-66-NH_2	DPV	2.0	[39]
Hg-film electrode	SWASV	0.84	[40]
Bi-film electrode	DPASV	5.0	[41]
Bare GCE	SWASV	68–87	[42]
SWNTs/Ag@ZnBDC/GCE	DPV	0.102	This work

4. Conclusions

In this study, a SWNTs/Ag@ZnBDC composite was successfully synthesised and characterised, demonstrating preserved ZnBDC crystallinity with the incorporation of AgNPs and SWNTs. The composite exhibited enhanced structural stability and improved conductivity, as confirmed by XRD, FTIR, FESEM, EDS, TGA/DTA, CV, and EIS analyses. Electrochemical sensing evaluation using the DPV method revealed that the SWNTs/Ag@ZnBDC/GCE electrode exhibited high selectivity and sensitivity toward Hg^{2+} ions, with an optimal sensing performance at pH 4. The sensor exhibited a linear response to Hg^{2+} concentrations in the range of 0.1–1.0 nM, with a strong correlation coefficient (R^2 = 0.9908). The LOD and LOQ were determined to be 0.102 nM and 0.39 nM, respectively, demonstrating high sensitivity comparable to or better than many previously reported electrochemical sensors. Furthermore, the sensor demonstrated reliable reproducibility and stability, highlighting the synergistic contribution of SWNTs and AgNPs in enhancing electron transfer and providing a large number of active sites. These results establish the SWNTs/Ag@ZnBDC composite as a promising candidate for the sensitive and selective detection of Hg^{2+} ions in environmental monitoring applications.

Author Contributions: Conceptualisation, G.A.B.; methodology, G.A.B., M.S.M. and B.H.; data curation, G.A.B. and B.H.; writing—original draft preparation, G.A.B., M.S.M. and B.H.; investigation, B.H.; supervision, M.K. and M.D.S.; project administration, M.K. and M.D.S.; resources, M.K. and M.D.S.; funding acquisition, M.K.; writing—review and editing, M.K. and M.D.S. All authors have read and agreed to the published version of the manuscript.

Funding: This research was supported by the National Research Foundation (NRF) of Korea grant funded by the Korea Government (NRF-2021R1A2C2094641).

Data Availability Statement: The original contributions presented in this study are included in the article.

Conflicts of Interest: The authors declare no conflicts of interest.

References

1. Deng, H.; Tu, Y.; Wang, H.; Wang, Z.; Li, Y.; Chai, L.; Zhang, W.; Lin, Z. Environmental behavior, human health effect and pollution control of heavy metal (loid) s towards full life cycle processes. *Eco-Environ. Health* **2022**, *1*, 229–243. [CrossRef]
2. Cheng, Z.; Wei, J.; Gu, L.; Zou, L.; Wang, T.; Chen, L.; Li, Y.; Yang, Y.; Li, P. DNAzyme-based biosensors for mercury (II) detection: Rational construction, advances and perspectives. *J. Hazard. Mater.* **2022**, *431*, 128606. [CrossRef]
3. Tuzen, M.; Sarı, A.; Mogaddam, M.R.A.; Kaya, S.; Katin, K.; Altunay, N. Synthesis of carbon modified with polymer of diethylenetriamine and trimesoyl chloride for the dual removal of Hg (II) and methyl mercury ([CH_3Hg]+) from wastewater: Theoretical and experimental analyses. *Mater. Chem. Phys.* **2022**, *277*, 125501. [CrossRef]
4. Shakeel, S.; Talpur, F.N.; Sirajuddin; Anwar, N.; Iqbal, M.A.; Ibrahim, A.; Afridi, H.I.; Unar, A.; Khalid, A.; Ahmed, I.A.; et al. Xanthan gum-mediated silver nanoparticles for ultrasensitive electrochemical detection of Hg^{2+} ions from water. *Catalysts* **2023**, *13*, 208. [CrossRef]
5. Singh, G.; Sushma; Priyanka; Diksha; Mohit; Gupta, S.; Esteban, M.A.; Espinosa-Ruíz, C.; González-Silvera, D. Designing of thiosemicarbazone-triazole linked organotriethoxysilane as UV-Visible and fluorescence sensor for the selective detection of Hg^{2+} ions and their cytotoxic evaluation. *J. Mol. Struct.* **2022**, *1255*, 132446. [CrossRef]
6. Ariño, C.; Banks, C.E.; Bobrowski, A.; Crapnell, R.D.; Economou, A.; Królicka, A.; Pérez-Ràfols, C.; Soulis, D.; Wang, J. Electrochemical stripping analysis. *Nat. Rev. Methods Primers* **2022**, *2*, 62. [CrossRef]
7. Khan, U.; Nairan, A.; Gao, J.; Zhang, Q. Current progress in 2D metal–organic frameworks for electrocatalysis. *Small Struct.* **2023**, *4*, 2200109. [CrossRef]
8. Knebel, A.; Caro, J. Metal–organic frameworks and covalent organic frameworks as disruptive membrane materials for energy-efficient gas separation. *Nat. Nanotechnol.* **2022**, *17*, 911–923. [CrossRef] [PubMed]
9. Liu, H.; Cheng, M.; Liu, Y.; Wang, J.; Zhang, G.; Li, L.; Du, L.; Wang, G.; Yang, S.; Wang, X. Single atoms meet metal–organic frameworks: Collaborative efforts for efficient photocatalysis. *Energy Environ. Sci.* **2022**, *15*, 3722–3749. [CrossRef]
10. Zheng, M.; Chen, J.; Zhang, L.; Cheng, Y.; Lu, C.; Liu, Y.; Singh, A.; Trivedi, M.; Kumar, A.; Liu, J. Metal organic frameworks as efficient adsorbents for drugs from wastewater. *Mater. Today Commun.* **2022**, *31*, 103514. [CrossRef]
11. Bodkhe, G.A.; Hedau, B.S.; Deshmukh, M.A.; Patil, H.K.; Shirsat, S.M.; Phase, D.M.; Pandey, K.K.; Shirsat, M.D. Detection of Pb (II): Au Nanoparticle Incorporated CuBTC MOFs. *Front. Chem.* **2020**, *8*, 803. [CrossRef]
12. Bodkhe, G.A.; Hedau, B.S.; Deshmukh, M.A.; Patil, H.K.; Shirsat, S.M.; Phase, D.M.; Pandey, K.K.; Shirsat, M.D. Selective and sensitive detection of lead Pb (II) ions: Au/SWNT nanocomposite-embedded MOF-199. *J. Mater. Sci.* **2021**, *56*, 474–487. [CrossRef]
13. Nivetha, R.; Gothandapani, K.; Raghavan, V.; Van Le, Q.; Pitchaimuthu, S.; Muthuramamoorty, M.; Pandiaraj, S.; Alodhayb, A.; Kwan Jeong, S.; Nirmala Grace, A. Nano-MOF-5 (Zn) Derived porous carbon as support electrocatalyst for hydrogen evolution reaction. *ChemCatChem* **2021**, *13*, 4342–4349. [CrossRef]
14. Song, Y.; Gong, C.; Su, D.; Shen, Y.; Song, Y.; Wang, L. A novel ascorbic acid electrochemical sensor based on spherical MOF-5 arrayed on a three-dimensional porous carbon electrode. *Anal. Methods* **2016**, *8*, 2290–2296. [CrossRef]
15. Petit, C.; Bandosz, T.J. Enhanced adsorption of ammonia on metal-organic framework/graphite oxide composites: Analysis of surface interactions. *Adv. Funct. Mater.* **2010**, *20*, 111–118. [CrossRef]
16. Bodkhe, G.A.; More, M.S.; Umar, A.; Ibrahim, A.A.; Siva, S.; Deshmukh, M.A.; Ingle, N.N.; Gaikwad, D.K.; Tsai, M.-L.; Hianik, T.; et al. Enhanced detection of heavy metal ions using Ag nanoparticles and single-walled carbon nanotubes within Cu-based metal-organic frameworks. *J. Environ. Chem. Eng.* **2024**, *12*, 113024. [CrossRef]
17. Yadav, D.K.; Ganesan, V.; Marken, F.; Gupta, R.; Sonkar, P.K. Metal@ MOF materials in electroanalysis: Silver-enhanced oxidation reactivity towards nitrophenols adsorbed into a zinc metal organic framework—Ag@ MOF-5 (Zn). *Electrochim. Acta* **2016**, *219*, 482–491. [CrossRef]

18. Panella, B.; Hirscher, M.; Pütter, H.; Müller, U. Hydrogen adsorption in metal–organic frameworks: Cu-MOFs and Zn-MOFs compared. *Adv. Funct. Mater.* **2006**, *16*, 520–524. [CrossRef]
19. Li, H.; Eddaoudi, M.; O'Keeffe, M.; Yaghi, O.M. Design and synthesis of an exceptionally stable and highly porous metal-organic framework. *Nature* **1999**, *402*, 276–279. [CrossRef]
20. Bodkhe, G.A.; Siva, S.; Gaikwad, D.K.; Tsai, M.-L.; Hianik, T.; Kim, M.; Shirsat, M.D. Ag nanoparticles incorporated metal organic framework (Ag@ ZnBDC): Highly sensitive and selective detection of Hg^{2+} ions. *J. Phys. Chem. Solids* **2024**, *193*, 112142. [CrossRef]
21. Munawar, T.; Bashir, A.; Mukhtar, F.; Nadeem, M.S.; Manzoor, S.; Ashiq, M.N.; Khan, S.A.; Koc, M.; Iqbal, F. Scalable synthesis of MOFs-derived ZnO/C nanohybrid: Efficient electrocatalyst for oxygen evolution reaction in alkaline medium. *J. Korean Ceram. Soc.* **2023**, *60*, 918–934. [CrossRef]
22. Bodkhe, G.A.; Khandagale, D.D.; More, M.S.; Deshmukh, M.A.; Ingle, N.N.; Sayyad, P.W.; Mahadik, M.M.; Shirsat, S.M.; Al-Buriahi, M.S.; Tsai, M.L.; et al. Ag@MOF-199 Metal Organic Framework for Selective Detection of Nickel Ions in Aqueous Media. *Ceram. Int.* **2023**, *49*, 6772–6779. [CrossRef]
23. Rahmani, M.; Ghafoorifard, H.; Afrang, S.; Ahmadi, M.T.; Rahmani, K.; Ismail, R. Effect of solution pH and adsorbent concentration on the sensing parameters of TGN-based electrochemical sensor. *IET Nanobiotechnol.* **2019**, *13*, 584–592. [CrossRef] [PubMed]
24. Huang, J.; Yuan, F.; Zeng, G.; Li, X.; Gu, Y.; Shi, L.; Liu, W.; Shi, Y. Influence of pH on heavy metal speciation and removal from wastewater using micellar-enhanced ultrafiltration. *Chemosphere* **2017**, *173*, 199–206. [CrossRef] [PubMed]
25. Maity, S.; Deshmukh, S.; Roy, S.S.; Dhar, B.B. Selenium-doped Graphite for Electrochemical Sensing and Adsorption of Hg (II) and Cd (II) Ions. *ChemElectroChem* **2023**, *10*, e202201044. [CrossRef]
26. Liu, T.; Xue, Q.; Jia, J.; Liu, F.; Zou, S.; Tang, R.; Chen, T.; Li, J.; Qian, Y. New insights into the effect of pH on the mechanism of ofloxacin electrochemical detection in aqueous solution. *Phys. Chem. Chem. Phys.* **2019**, *21*, 16282–16287. [CrossRef]
27. Bodkhe, G.A.; Siva, S.; Cong, C.; Castro, I.J.L.; Kim, S.H.; Kim, M. Electrohydrodynamically configured aflatoxin B1 probing field effect transistor biosensor. *Microchem. J.* **2025**, *215*, 114385. [CrossRef]
28. Siva, S.; Bodkhe, G.A.; Cong, C.; Kim, S.H.; Kim, M. Electrohydrodynamic-printed ultrathin $Ti_3C_2T_x$-MXene field-effect transistor for probing aflatoxin B1. *Chem. Eng. J.* **2024**, *479*, 147492. [CrossRef]
29. Zorn, M.E.; Gibbons, R.D.; Sonzogni, W.C. Evaluation of approximate methods for calculating the limit of detection and limit of quantification. *Environ. Sci. Technol.* **1999**, *33*, 2291–2295. [CrossRef]
30. Singh, S.; Numan, A.; Zhan, Y.; Singh, V.; Van Hung, T.; Nam, N.D. A novel highly efficient and ultrasensitive electrochemical detection of toxic mercury (II) ions in canned tuna fish and tap water based on a copper metal-organic framework. *J. Hazard. Mater.* **2020**, *399*, 123042. [CrossRef]
31. Zhang, L.; Pu, Y.; Xu, W.; Peng, J.; Liu, Y.; Du, H. A ratiometric electrochemical sensor for simultaneous detection of multiple heavy metal ions in water and herbal medicines based on methylene blue-functionalised metal–organic framework. *Microchem. J.* **2024**, *201*, 110542. [CrossRef]
32. Shao, Z.; Di, K.; Ding, L.; You, F.; Fan, C.; Wang, K. Amino-enriched Zn-MOFs with self-reduction for energy-free simultaneous removal and electrochemical detection of heavy metal ions in the aquatic environment. *Anal. Chim. Acta* **2025**, *1333*, 343408. [CrossRef]
33. Baghayeri, M.; Amiri, A.; Moghaddam, B.S.; Nodehi, M. Cu-Based MOF for simultaneous determination of trace Tl (I) and Hg (II) by stripping voltammetry. *J. Electrochem. Soc.* **2020**, *167*, 167522. [CrossRef]
34. Chen, X.; Liu, Y.; Ke, X.-X.; Weerasooriya, R.; Li, H.; Wang, L.-C.; Wu, Y.-C. A green method to synthesise AuNPs/mpg-C_3N_4 nanocomposites for constructing anti-interference electrochemical sensing interface toward methylmercury. *J. Alloys Compd.* **2021**, *853*, 157365. [CrossRef]
35. Kim, M.-H.; Hedau, B.S.; Sayyad, P.W.; Kim, J.; Ha, T.-J. Electrochemical environmental sensors based on La-doped zeolitic imidazolate framework-67 functionalised with L-cysteine for simultaneous detection of Cd^{2+} and Hg^{2+}. *Appl. Surf. Sci.* **2025**, *689*, 162549. [CrossRef]
36. Shejwal, N.N.; Patil, S.S.; Lanke, H.R.; Kamble, R.B.; Gole, P.V.; Shirsat, M.D. Ag-modified La-succinate composite as a novel electrochemical sensor for Hg^{2+} ion detection. *J. Solid State Electrochem.* **2025**, 1–12. [CrossRef]
37. Bodkhe, G.A.; More, M.S.; Hashem, M.; Fouad, H.; Siva, S.; Deshmukh, M.A.; Ingle, N.N.; Kim, M.; Shirsat, M.D. Hg^{2+} ions sensor: Single walled carbon nanotubes incorporated Zn-metal organic framework. *J. Nanoelectron. Optoelectron.* **2023**, *18*, 993–1001. [CrossRef]
38. Pei, L.; Yang, H.; Chen, S.; Wang, L. UiO-66-NHC (S) NHMe/three-dimensional macroporous carbon for removal and electrochemical detection of Cd^{2+}, Pb^{2+}, Cu^{2+}, and Hg^{2+}. *Ind. Eng. Chem. Res.* **2022**, *61*, 1588–1595. [CrossRef]
39. Lu, M.; Deng, Y.; Luo, Y.; Lv, J.; Li, T.; Xu, J.; Chen, S.-W.; Wang, J. Graphene aerogel–metal–organic framework-based electrochemical method for simultaneous detection of multiple heavy-metal ions. *Anal. Chem.* **2018**, *91*, 888–895. [CrossRef]

40. Economou, A.; Fielden, P.R. Mercury film electrodes: Developments, trends and potentialities for electroanalysis. *Analyst* **2003**, *128*, 205–213. [CrossRef]
41. Clavijo Morales, J.A.; Zea Ramírez, H.R. Simultaneous quantification of Hg (II) and Pb (II) by square wave anodic stripping voltammetry using Bi/graphite electrode. *Heliyon* **2024**, *10*, e34656. [CrossRef]
42. Tonle, I.K.; Ngameni, E.; Walcarius, A. Preconcentration and voltammetric analysis of mercury (II) at a carbon paste electrode modified with natural smectite-type clays grafted with organic chelating groups. *Sens. Actuators B Chem.* **2005**, *110*, 195–203. [CrossRef]

Disclaimer/Publisher's Note: The statements, opinions and data contained in all publications are solely those of the individual author(s) and contributor(s) and not of MDPI and/or the editor(s). MDPI and/or the editor(s) disclaim responsibility for any injury to people or property resulting from any ideas, methods, instructions or products referred to in the content.